ADVANCES IN ATMOSPHERIC SCIENCES, VOL. 42, FEBRUARY 2025, 313–326

• **Original Paper** •

Energy Meteorology for the Evaluation of Solar Farm Thermal Impacts on Desert Habitats※

Carlos F. M. COIMBRA*

Department of Mechanical and Aerospace Engineering, Jacobs School of Engineering, Center of Excellence in Renewable Resource Integration and Center for Energy Research, University of California San Diego, La Jolla, CA 92093, *USA*

(Received 24 June 2024; revised 20 August 2024; accepted 15 September 2024)

ABSTRACT

This work addresses challenges and opportunities in the evaluation of solar power plant impacts, with a particular focus on thermal effects of solar plants on the environment and vice-versa. Large-scale solar power plants are often sited in arid or desert habitats, which tend to include fauna and flora that are highly sensitive to changes in temperature and humidity. Our understanding of both shortwave (solar) and longwave (terrestrial) radiation processes in solar power plants is complete enough to render the modeling of radiation fluxes with high confidence for most applications. In contrast to radiation, the convective environment in large-scale solar power plants is much more difficult to characterize. Wind direction, wind speed, turbulence intensity, dust concentration, ground condition, panel configuration density, orientation and distribution throughout the solar field, all affect the local environment, the balance between radiation and convection, and in turn, the performance and thermal impact of solar power plants. Because the temperatures of the two sides of photovoltaic (PV) panels depend on detailed convection–radiation balances, the uncertainty associated with convection affects the heat and mass transfer balances as well. Those balances are critically important in estimating the thermal impact of large-scale solar farms on local habitats. Here we discuss outstanding issues related with these transfer processes for utility-scale solar generation and highlight potential pathways to gain useful knowledge about the convective environment directly from solar farms under operating conditions.

Key words: environmental impact, solar farms, thermal balances, shortwave and longwave radiation, convection

Citation: Coimbra, C. F. M., 2025: Energy meteorology for the evaluation of solar farm thermal impacts on desert habitats. *Adv. Atmos. Sci.*, **42**(2), 313−326, https://doi.org/10.1007/s00376-024-4242-3.

Article Highlights:

- Detailed thermal balances yield alternative methods to determine convective effects on PV panels.
- Experimental and modeling methods are combined to determine the impacts of solar farms.
- A methodology to classify microclimates according to the effective optical depth of the sky is proposed.
- Global heat transfer coefficients can be determined from solar farm operating conditions.
- Understanding the impacts of solar farms on sensitive desert habitats requires detailed thermal balances at the panel scale.

1. Introduction

In its narrower scope, "Energy Meteorology" refers to the interaction between weather and the utilization of energy, especially renewable energy, and more particularly solar and wind energy. This terminology entered the renewable energy lexicon in the past few decades mostly to highlight the importance of cloud positioning with respect to solar power receivers on the ground. Cloud positioning is seldom of importance to meteorologists, but the determination of cloud position, velocity and optical depth is the primary concern of solar resourcing and forecasting engineers. In its broader scope, "Energy Meteorology" applies to any effect that weather has on power generation, transmission and distribution systems, including effects on the efficiency of cooling towers in fossil fueled thermoelectric power plants, evaporation and precipitation in hydroelectric dams, downstream flow effects of wind farms, heat rejection from nuclear power plants, as well as weather impacts on transmission lines, transformers, etc. In this work, we restrict the use of "Energy Meteorology" to solar generation, but expand its usual scope to include not only the effects of weather on

※ This paper is a contribution to the special topic on Solar Energy Meteorology.

* Corresponding author: Carlos F. M. COIMBRA
Email: ccoimbra@ucsd.edu

solar power plants, but also the reverse effect—namely, the effect of solar power plants on the local environment. The impact of large-scale solar generation on arid, semi-arid and desert areas is still poorly understood (Hernandez et al., 2014). While there is little hope to address all issues related to the potential (positive, negative or negligible) impacts of solar farms on sensitive habitats within a short paper, here we aim to provide a general view on how to reduce the uncertainty in determining thermal effects from solar plants on the local environment. This work is also a call for solar power farm designers, owners, managers and operators to invest in suitable telemetry that can resolve many of the outstanding issues pertaining to the actual thermal impact of solar power plants on the local environment. It behooves us in the solar energy research community to answer concerns and criticisms that the solar power industry encounters with the best possible science. It could very well be that the net thermal impact of large-scale power plants is minimal, or even benign, but the conflicting results reported in the research literature point at the need to study the problem from the standpoint of fundamental thermal balances.

A simple practical example illustrates the local thermal balances needed to properly study the relationship between the different heat and mass transfer processes at play. While this simple model can be substantially improved, the goal here is not to provide a definitive model, but to motivate further research in the field, as well as to point at potential pathways to combined field experiments and detailed modeling for more robust understanding of the processes at play.

The uncertainty in environmental conditions, particularly with respect to convective heat transfer coefficients, is typically too large to provide definitive answers, which leads to different studies arriving at different impacts in terms of local thermal anomalies caused by solar farms. For example Nemet (2009) concludes that the low shortwave reflectivity (albedo) of photovoltaic (PV) power plants reduces the carbon emissions offset of PV power production by 3%. This implies that at least part of the solar conversion efficiency is offset by the albedo replacement effect. Barron-Gafford et al. (2016) studied the heat island effect of PV solar farms, reporting increased temperature levels at night of ~3–4 K, in direct opposition to a previous study that found a net cooling effect of PV solar farms overall (Masson et al., 2014). An overall cooling effect of ~3 K was observed for solar heliostat fields on desert environments by Millstein and Menon (2011). Hu et al. (2016) studied the impact of widespread PV deployment on the global climate, whereas Hernandez et al. (2014) provide a broad overview of the several types of environmental impacts resulting from solar power utilization. The present work focuses on thermal effects only, and provides detailed thermal balance models for PV power plants that can be easily modified to heliostat fields.

Current models for the different heat transfer modes are likely just accurate enough to provide information for designing more detailed field experiments. Many of the key factors that influence the environmental impact of solar power plants must be measured locally for a complete picture. Experimental data are needed during daytime and nighttime under real operating conditions and for different locations within the solar farms. As it will be made clear below, both longwave and shortwave radiation balances need to be carefully considered in addition to the poorly characterized convective environment. The work by Fan and Huang (2021) emphasizes the importance of proper modeling of longwave radiation fluxes to investigate the thermal impact of solar farms through remote sensing [see also Larson et al. (2020) for a more detailed model of the longwave fluxes]. Smith et al. (2022b) discuss the importance of panel height in enhancing heat rejection by convection and thus increasing plant efficiency.

Recent developments [see, e.g., Smith et al. (2022a)] have provided both wind tunnel and simulation results that allow for better estimation of convective heat transfer coefficients at the scale of the plant, and in some cases within the scale of the panel arrays. These results not only help us design better solar farms, but also allow for the evaluation of the overall effect of large-scale farms on the local environment. Similarly, recent detailed calibration of downwelling longwave radiation (DLR) models (Matsunobu and Coimbra, 2024) allow for improved consideration of thermal balances for both daytime and nighttime conditions.

Because both the design and the environmental impact assessment of solar farms require knowledge of thermal, radiative and optical properties of materials, heat and mass transfer rates, meteorology, plus atmospheric and solar radiation resourcing, it is unlikely that a single short paper can contain the necessary information pertinent to the entire thermal balance process. This work is written for meteorologists and solar engineering researchers who are interested in branching out from their respective research silos. The analysis aims at providing a research primer for those interested in exploring new research opportunities in energy meteorology applied to solar farms. The arguments we make follow an application to simple geometric configuration that can be expanded to progressively more realistic conditions through additional research, complemented by directed modeling and field experiments.

2. The problem at hand

2.1. *The object of study*

Modern utility-scale solar fields can be broadly classified as either non-concentrated (one-sun) or concentrated solar power fields. The first category includes tracking and non-tracking flat panels based on silicon of thin film PV cells, which are by far the most common solar farms deployed today. Concentrated technologies include a variety of technologies varying from central towers surrounded by heliostat fields to fields of solar trough concentrators, among many other possible configurations. The thermal balances described in this work are directed at one-sun solar farms, but they can be easily adapted to heliostat fields, as most

heliostats are essentially flat sheets of glass (curved, but with very large radii of curvature), and therefore can be treated as glass panes with reflective back-painted films.

The irreducible element of a non-concentrating PV solar farm is the PV panel, which includes a planar arrangement of solar cells encapsulated by a plastic (typically made of crosslinked ethylene vynil acetate, or EVA) on both sides and UV-protected by a sheet of either glass, Tedlar or polycarbonate plastic on the top side. On the back side of the panel, a thin backsheet insulation of TPT (Tedlar Polyester Tedlar), PVF (polyvinyl fluoride) or PET (polyethylene terephthalate) is used for structural and weather protection but, most importantly, as a heat sink during daytime. Table 1 shows the effective thermal properties for the cross-section of a panel composed of glass, EVA, a solar cell layer and PVF. The dataset in Table 1 includes typical dimensions and properties adapted from various sources, but mostly from large-scale manufacturer specifications and the works by Notton et al. (2005) and Wang et al. (2023). Note that the very thin solar cell is a composite of semiconductor and conductor parts and therefore has effective thermal properties that lie in between those of its pure component substances.

If the glass pane is assumed opaque and conduction through the panel is the dominant mode of heat transfer through the solid layers of the panel, a quasi-steady (constant) net heat transfer flux W m^{-2} passing through the thickness of the panel results in a difference between the top temperature of the glass T_{top} and the bottom temperature of the backsheet insulation T_{bottom} given by:

$$q_{cond} = \frac{T_{top} - T_{bottom}}{R_{cond}} , \quad (1)$$

where the equivalent thermal resistance for conduction across the thickness of the panel is

$$R_{cond} = \sum_{i}^{5} \frac{\delta_i}{k_i} . \quad (2)$$

If we take the thickness and thermal conductivity values used by Wang et al. (2023), we can calculate $R_{C,eq} \sim 0.01$ K m^2 W^{-1}. This effective thermal resistance value is to be interpreted in steady-state as: for every 100 W of heat flux through the panel, there is 1 K of temperature difference between T_{top} and T_{bottom}. Note that this value neglects contact resistances between the elements of the panel, and those contact resistances could be significant, especially in the evacuated space between the encapsulation and the solar cell. At nighttime, when there is no shortwave radiation, the heat balance is simply

$$q_{cond} = q_{top} = q_{bottom} , \quad (3)$$

where q_{top} and q_{bottom} are the net heat fluxes (balances between radiosity, irradiation and convective heat transfer) in the top and bottom sides of the panel. Nighttime conditions are such that the difference between T_{top} and T_{bottom} is often small in comparison to differences between either side and the surrounding air temperature, but often $T_{top} < T_{bottom}$ due to the lower values of DLR from the atmosphere in comparison to the upwelling longwave radiation (ULR) from the ground. The correct estimation of T_{bottom} during both daytime and nighttime is important in evaluating heat and mass transfer from the surrounding soil, especially in sensitive arid habitats. The correct estimation of soil moisture content and temperature should be given considerable thought, and careful experimentation during solar plant operating conditions should be carried out. This is particularly important because latent heat fluxes can affect thermal balances substantially given the high value of the enthalpy of vaporization for water.

In the presence of shortwave (solar) radiation (daytime), the heat flux imbalance must account for the amount of solar power converted to electricity. Here, we denote shortwave radiation the entire solar radiation spectrum with wavelengths smaller than 4 μm. Terrestrial or atmospheric radiation is considered longwave radiation, and refers to wavelengths larger than 4 μm [see, e.g., Li and Coimbra (2019)]. Direct application of the First Law of Thermodynamics to a quasi-steady control volume containing composite and opaque layers of material yields

$$q_{in} - q_{out} - \dot{w}_{PV} = 0 , \quad (4)$$

where $\dot{w}_{PV}$ is the power per unit of area generated by the PV panel, which can be approximated as

$$\dot{w}_{PV} = \eta_{PV} G_{sw,top} , \quad (5)$$

where $G_{sw,top}$ is the shortwave radiation flux that strikes on the top surface of the panel and η_{PV} is the PV conversion efficiency to electric power of the shortwave radiation flux that arrives at the PV panel per unit of area (this term, i.e., the PV conversion efficiency of the panel will be more carefully defined in subsection 3.3). Different than the balance for longwave radiation, the glass cover and the encapsulation layers

Table 1. Thermal properties of the different layers of a typical PV panel.

Layer	Material	δ (mm)	ρ (kg m^{-3})	k (W m^{-1} K)	c (J kg^{-1} K)
1	glass	3.0–3.5	2300–3000	0.7	500–790
2	EVA	0.5	969	0.311	2,090
3	solar cell	0.21	2330	130–150	677–836
4	EVA	0.50	960	0.311	2090
5	PVF	0.30	1200	0.15	1250

cannot be considered opaque to shortwave radiation for obvious reasons. The transmissivity to normally incident shortwave radiation of a 3-mm-thick commercial glass with low iron content ranges from 0.85–0.90, and the absorptivity of normally incident shortwave radiation by PV cells is about 0.90–0.95, which yields an effective system product $(\tau\alpha)_{\text{eff}}$ close to 0.9 for normal incidence. This value can be corrected for non-normal incidence as described in subsection 3.3.

A simple steady-state power flux balance for the PV cell is thus (Duffie and Beckman, 2013)

$$[(\tau\alpha)_{\text{eff}} - \eta_{\text{PV}}]G_{\text{sw,top}} = U(T_{\text{cell}} - T_e)\,, \tag{6}$$

where U is the global heat transfer coefficient (including conduction, convection and radiation) that accounts for all thermal losses from the cell to the environment at T_e. We will return to the problem of estimating the value of U later, but let us first consider a simpler blackbody panel model that allows us to better understand how the effective convective heat transfer coefficients h_c can be estimated from accurate measurements of temperature and radiative fluxes, which are both more precise and accurate than the estimation of convection fluxes in open spaces.

2.2. *A simple blackbody panel model*

Consider the 2D geometry of a panel described in Fig. 1. The panel casts a shadow of length L_{shaded} on the ground when the direct beam angle of incidence is θ with the normal $\vec{n}$ to the panel. Assume first that the different layers shown in the figure inset are all opaque and perfectly absorbing and emitting. In this preliminary model, all surfaces are assumed black to both shortwave and longwave radiation, and have thermal properties corresponding to the following specific values in Table 1 (Wang et al., 2023): $\delta_{\text{glass}} = 3.2$ mm, $\rho_{\text{glass}} = 2{,}450$ kg m^{-3}, and $k_{\text{cell}} = 130$ W m^{-1} K. The effective thermal conductivity for the panel of thickness $\delta = 4.71$ mm is thus $k_{\text{eff}} = 0.481$ W m^{-1} K. Equation (3) is written as

$$q_{\text{top}} = q_{\text{bottom}} = k_{\text{eff}}\left(\frac{T_{\text{top}} - T_{\text{bottom}}}{\delta}\right), \tag{7}$$

where q_{top} is, again, the net flux from both convection and radiation on the top of the panel and q_{bottom} is the net heat flux at the bottom. Heat balances for the top and bottom interfaces yield (see Fig. 1)

$$q_{\text{top}} = G_{\text{top}} - J_{\text{top}} - \overline{h}_{c,\text{top}}(T_{\text{top}} - T_e)\,, \tag{8}$$

and

$$q_{\text{bottom}} = J_{\text{bottom}} - G_{\text{bottom}} + \overline{h}_{c,\text{bottom}}(T_{\text{bottom}} - T_e)\,, \tag{9}$$

where G_{top} and G_{bottom} are the total irradiation fluxes including both shortwave (solar) and longwave (atmospheric and ground) radiation fluxes incident on either side of the panel surfaces. The radiosities J_{top} and J_{bottom} are simply the blackbody radiosities σT_{top}^4 and $\sigma T_{\text{bottom}}^4$ in this case. The shortwave irradiation fluxes include the direct beam, the circumsolar flux, the sky diffuse, and the ground reflected components. The longwave irradiation includes the radiation emitted by the atmosphere and incoming flux from the ground surfaces. In many circumstances, it is important to distinguish between the shaded and sunny portions of the ground, as temperature differences and soil humidity content variations can be significant.

Note that the formulation above assumes that there is a meaningful averaged value of the ambient (free stream) air temperature T_e that, combined with a suitable convective

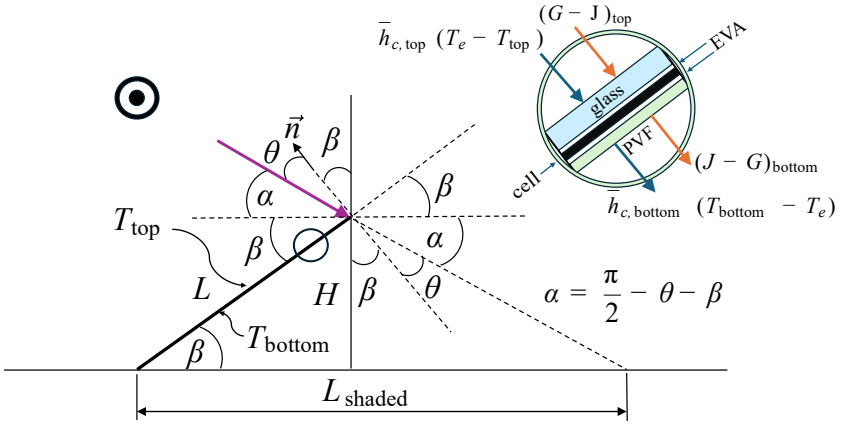

Fig. 1. Geometric configuration of a long (2D) array of PV panels facing the equator and sloped with an angle β with the horizontal. The solar beam strikes the panel with angle θ with respect to the normal to the top surface. At the moment depicted in this figure, the panel of length L casts a shade of length L_{shaded} on the ground. The circular inset shows the composition of the PV panel and both radiative and convective fluxes on each side of the panel. The inset shows a typical panel configuration with the PV cell encapsulated by EVA, a glass cover and a PVF backsheet. Note that the thicknesses showed in the inset are not to scale as both the PV cell and the layer of PVF are typically thinner than the encapsulation (see Table 1 for typical dimensions).

heat transfer coefficient $\overline{h}_{c,\text{side}}$, results in the correct estimation of convective effects for each surface of the panel. Lateral losses are justifiably neglected. In reality, the free-stream temperature T_e may differ considerably for the different sides of the panel, but the exact determination T_e is often done for multiple meteorological reasons at standard heights (e.g., at 2, 5, and 10 m from the ground surface), and not directly under and above the panels, and often far from the poorly characterized boundary layers in each side of the panel.

Combining Eqs. (7), (8), and (9), and solving for $\overline{h}_{c,\text{side}}$ gives us

$$\overline{h}_{c,\text{top}} = \frac{1}{(T_{\text{top}} - T_e)}\left[G_{\text{top}} - J_{\text{top}} - \frac{k_{\text{eff}}\,(T_{\text{top}} - T_{\text{bottom}})}{\delta}\right], \tag{10}$$

and

$$\overline{h}_{c,\text{bottom}} = \frac{1}{(T_{\text{bottom}} - T_e)} \times\left[G_{\text{bottom}} - J_{\text{bottom}} + \frac{k_{\text{eff}}\,(T_{\text{top}} - T_{\text{bottom}})}{\delta}\right]. \tag{11}$$

The remarkable feature of Eqs. (10) and (11) is that they estimate the values of $\overline{h}_{c,\text{side}}$ as algebraic relationships among easily measurable surface fluxes and temperatures, in addition to the surrounding air temperature T_e. This is one of the main technical points advanced in this work: flow-dependent variables such convective heat transfer coefficients are difficult to measure in a complex geometrical arrangement such as those found in solar power plants. Even averaged wind speed values are not easy to estimate over panels. However, the thermal balances of the panels themselves provide a straightforward way to estimate convective heat transfer coefficients from variables that are more easily measured on planes or surfaces, provided that the ambient air temperature is suitably defined and measured. Note also that these estimates are valid for both daytime and nighttime conditions. The two equations above provide separate opportunities to determine side-averaged values of $\overline{h}_{c,\text{side}}$ from measurements done on the top and bottom surface of a blackbody panel, and to check if the assumption of a single averaged value $\overline{h}_{c,\text{panel}}$ is justifiable.

If in addition to assuming that a single free-stream temperature T_e value is representative of the flow around the panel we further assume that $\overline{h}_{c,\text{side}} = \overline{h}_{c,\text{top}} = \overline{h}_{c,\text{bottom}}$, which is a common assumption made in most previous studies [see, for example, Notton et al. (2005) and references within], a direct subtraction of Eq. (9) from Eq. (8) yields

$$\overline{h}_{c,\text{black panel}} = \frac{(G_{\text{top}} + G_{\text{bottom}}) - (J_{\text{top}} + J_{\text{bottom}})}{(T_{\text{top}} + T_{\text{bottom}})}. \tag{12}$$

Equation (12) is a good starting point for our model because it estimates the model panel convective heat transfer coefficient based on the balance between shortwave (solar) and longwave (atmospheric+ground) fluxes, and easily measurable surface temperatures on both sides of the panel.

Another important feature of Eq. (12) is that it allows for both theoretical and experimental estimates of the irradiation fluxes. Experimentally, the irradiation fluxes can be measured by two sets of shortwave ($\lambda \lesssim 4$ μm) pyranometers and longwave ($\lambda \gtrsim 4$ μm) pyrheliometers mounted on the plan-of-array (POA) in each side of the panels. Average temperatures for the cover (top) and for the backsheet (bottom) can be be measured by thermocouples distributed over the surfaces. Very importantly, the temperatures are measured on surfaces with considerable thermal inertia, which greatly improves time-averaging of temperature readings. With these simple and readily available measurements and instruments, the effective convective heat transfer coefficients can be estimated with higher fidelity than simple correlations based on wind speed, and for the same mounting conditions of the PV array as well. Both the shortwave and the longwave irradiation fluxes can be estimated from models. In fact, estimating these fluxes is the chief objective of energy meteorology, as described in section 3. However, before we tackle the determination of the longwave and shortwave radiation fluxes, let us improve on the blackbody panel model by considering a gray panel with PV generation.

2.3. *A gray panel with PV generation*

Equations (10) and (11) provide a reasonable estimate for $\overline{h}_{c,\text{side}}$ for a black panel with no electric generation. Clearly, a real PV panel generates electricity during daytime and is not a blackbody, and thus the radiative fluxes and temperatures differ from the blackbody panel model. We will address some of the most important corrections now. To improve on the blackbody model we now consider a gray panel with power flux generation $\dot{w}_{\text{PV}}$. In this case, even under steady-state conditions, there is an imbalance between the top and bottom heat fluxes, as indicated in Eq. (4). Here, we apply the power balance to the entire panel, and not only to the cell:

$$q_{\text{top}} - q_{\text{bottom}} = \dot{w}_{\text{PV}}\,, \tag{13}$$

where, referring to Fig. 1,

$$q_{\text{top}} = G_{\text{top}} - J_{\text{top}} - \overline{h}_{c,\text{top}}\,(T_{\text{top}} - T_e)\,, \tag{14}$$

and

$$q_{\text{bottom}} = J_{\text{bottom}} - G_{\text{bottom}} + \overline{h}_{c,\text{bottom}}\,(T_{\text{bottom}} - T_e)\,. \tag{15}$$

Subtracting Eq. (15) from Eq. (14) and substituting Eq. (13) after assuming again that $\overline{h}_{c,\text{top}} = \overline{h}_{c,\text{bottom}}$, results in

$$\overline{h}_{c,\text{gray panel}} = \frac{(G_{\text{top}} + G_{\text{bottom}}) - (J_{\text{top}} + J_{\text{bottom}}) - \dot{w}_{\text{PV}}}{(T_{\text{top}} + T_{\text{bottom}})}, \tag{16}$$

which is analogous to Eq. (12), but differs from it in two distinct ways. First, is the obvious inclusion of the (negative) PV power flux term in the numerator. Second, the radiosities

in Eq. (16) are no longer blackbody radiosities of the form σT^4 but now include both the gray emission component $\varepsilon_{\text{side}}\sigma T_{\text{side}}^4$ and the reflected component $(1-\varepsilon_{\text{side}})G_{\text{side}}$, so that,

$$J_{\text{side}} = \varepsilon_{\text{side}}\sigma T_{\text{side}}^4 + (1-\varepsilon_{\text{side}})G_{\text{side}}\,, \tag{17}$$

where Kirchhoff's detailed radiative balance is implied for both shortwave and longwave properties.

The net radiative flux in each side is thus simply:

$$\begin{aligned} G_{\text{side}} - J_{\text{side}} &= G_{\text{side}} - \varepsilon_{\text{side}}\sigma T_{\text{side}}^4 - (1-\varepsilon_{\text{side}})G_{\text{side}} \\ &= \varepsilon_{\text{side}}\,(G_{\text{side}} - \sigma T_{\text{side}}^4)\,, \end{aligned} \tag{18}$$

and, therefore

$$\overline{h}_{c,\,\text{gray panel}} = \frac{(\varepsilon_{\text{top}}G_{\text{top}} + \varepsilon_{\text{bottom}}G_{\text{bottom}}) - (\varepsilon_{\text{top}}\sigma T_{\text{top}}^4 + \varepsilon_{\text{bottom}}\sigma T_{\text{bottom}}^4) - \dot{w}_{\text{PV}}}{(T_{\text{top}} + T_{\text{bottom}})}\,. \tag{19}$$

Although there are many assumptions embedded in Eq. (19), this equation provides a fairly good approximation for the panel convective heat transfer coefficient under both daytime and nighttime conditions. It also provides the means to determine the local convective heat transfer coefficient from either measurements or models, or from a combination of both empirical and model data. The formulation above allows for consideration of selective properties, i.e., different radiative properties for shortwave and longwave fluxes, which we will consider next.

3. The critical role of energy meteorology

In this section we discuss effective models for the irradiation fluxes and identify challenges and opportunities for energy meteorologists to better characterize the thermal impact of large-scale solar power plants on sensitive habitats. Estimating the thermal impact requires estimating the radiative fluxes on both sides of the PV panels during power generation and during nighttime, when the panels may obstruct direct longwave and convective exchanges between the atmosphere and the ground.

3.1. *Longwave irradiance ($\lambda > 4\mu m$) under clear-sky conditions*

Models for DLR from the atmosphere's main constituents have been developed for almost 100 years (Berdahl, 2021; Li et al., 2018; Martin and Berdahl, 1984). For clear-sky conditions, the agreement between two-flux, line-by-line (LBL) spectral models for standard atmospheric profiles of temperature and species concentrations with experimentally determined values measured at ground level is truly astonishing [see, e.g., Li et al. (2018), Li and Coimbra (2019), Larson et al. (2020), and Matsunobu and Coimbra (2024)]. If broadband radiative property values for the surfaces involved are representative of the entire longwave spectrum, the longwave irradiance flux from the atmosphere on a horizontal plane can be readily estimated as

$$G_{\text{LW, horizontal}} = \varepsilon_{\text{LW, sky}}\,\sigma T_e^4\,, \tag{20}$$

where the subscripts "LW" and "horizontal" correspond to longwave and horizontal irradiance, respectively, T_e is the ambient temperature of the air at the screening height (1.5 to 2.0 m). The daytime emissivity of the clear sky is given by Matsunobu and Coimbra (2024):

$$\varepsilon_{\text{LW, clear day}} = 0.600 + 1.652\sqrt{p_w} + 0.150\,(e^{-z/H_o} - 1)\,, \tag{21}$$

where z is the altitude of the site in meters; H_o is 8500 m; p_w is the dimensionless partial pressure of water vapor in air at the screening height in pascals, P_w, divided by P_o, the nominal atmospheric pressure at sea level, 101 325 Pa. For low-altitude sites ($z \ll 1000$ m), the altitude correction may be neglected. For nighttime, the first constant in Eq. (21) is, on average, larger by a near constant value due to thermal inversions in the atmosphere, such that $\varepsilon_{\text{clear night}} = \varepsilon_{\text{clear day}} + 0.035$, as discussed in Li et al. (2017).

The coefficients in Eq. (21) result from recalibration and detailed sensitivity analyses of multidecadal data collection on several locations and microclimates spread across the United States (Matsunobu and Coimbra, 2024), but the coefficients hold remarkably well for tropical and polar regions as well [see discussion below and the works by Shakespeare and Roderick (2021), Shakespeare and Roderick (2022), Berdahl (2021), and Matsunobu and Coimbra (2024)]. Equation (20) gives the downwelling longwave irradiation on a horizontal surface at ground level. For a solar panel sloped at angle β with the horizontal, the longwave irradiation is a mixture of ground irradiation and sky irradiation, and the fraction of each is determined by view (configuration) factors. View factors are used for Lambertian (diffuse) radiation between surfaces that receive diffuse heat fluxes and are at uniform temperatures. Longwave radiation approximates these conditions, at least for the purposes intended here. After application of the reciprocity rule and cancellation of areas, the view factors of interest to a flat panel as depicted in Fig. 1 are:

$$F_{\text{top–sky}} = \frac{1+\cos\beta}{2}\,, \tag{22}$$

$$F_{\text{top–ground}} = \frac{1-\cos\beta}{2}\,, \tag{23}$$

$$F_{\text{bottom–sky}} = \frac{1-\cos\beta}{2}\,, \tag{24}$$

$$F_{\text{bottom}-\text{sunny}} = \frac{\left[\dfrac{\sin\beta[1-\sin(\beta+\theta)]}{\cos(\beta+\theta)}\right]}{2}, \quad (25)$$

$$F_{\text{bottom}-\text{shaded}} = \frac{\left[1+\cos\beta+\dfrac{\sin\beta[\sin(\beta+\theta)-1]}{\cos(\beta+\theta)}\right]}{2}, \quad (26)$$

where the portion of the ground that is denominated sunny behind the panel is the portion beyond the length L_{shaded} in the sketch. The ground in the front of the panel is assumed to be exposed to direct sunlight in these equations. The view factors above are valid for a single, long array, and can easily be derived using Hottel's crossed string method [see, e.g., Mills and Coimbra (2015)]. If the panel arrays are closer to each other, more elaborate view factors that take into consideration the other arrays should be used [see, e.g., Fathi and Samer (2016) and Nassar et al. (2022)].

With proper view factors calculated, and taking the view factor reciprocity rule into account, the clear-sky longwave irradiance on the top surface of the panel is

$$G_{\text{LW,top}} = F_{\text{top}-\text{sky}}\, G_{\text{LW,horizontal}} + F_{\text{top}-\text{ground}}\, \varepsilon_{\text{LW,sunny}} \sigma T_{\text{sunny}}^4, \quad (27)$$

where the subscript "sunny" is used here exclusively for the portion of the ground that is exposed to direct sunlight. It is generally assumed that the longwave emissivity of the ground surfaces $\varepsilon_{\text{LW,sunny}}$ and $\varepsilon_{\text{LW,shaded}}$ are equal to each other and near unity, but this assumption must be further studied, especially in the presence of humid soil. Equivalently, the clear-sky longwave irradiation at the bottom side of the panel is

$$\begin{aligned} G_{\text{LW,bottom}} = {} & F_{\text{bottom}-\text{sky}}\, G_{\text{LW,horizontal}} + \\ & F_{\text{bottom}-\text{sunny}}\, \varepsilon_{\text{LW,sunny}} \sigma T_{\text{sunny}}^4 + \\ & F_{\text{bottom}-\text{shaded}}\, \varepsilon_{\text{LW,shaded}} \sigma T_{\text{shaded}}^4, \end{aligned} \quad (28)$$

where T_{shaded} refers to the temperature of the shaded soil behind the panel.

It stands to reason that large-scale solar power plants should be deployed in places where a vast majority of the days are clear of clouds. However, and with very few exceptions, even the most arid deserts experience cloudy days. Some, like parts of the Mojave desert, observe monsoon clouds during the high-price energy season. The clear-sky denomination implies everything else in the atmosphere but clouds. Clouds have a substantial effect on the magnitude of the longwave irradiation observed on the ground level. As a very simple measure of this effect, consider a cold and dry day at sea level where relative humidity is very low. Under these circumstances, the value of p_w is very small, and the effective emissivity of the daytime clear sky approaches 0.600. The effective temperature of the sky is 12% lower than the ambient temperature in kelvins. For an average global temperature of 289 K, this means that the effective sky temperature is about 254 K, or 35 degrees below the ambient air temperature at the screening height. The DLR on a horizontal plane under these clear-sky conditions ($T_e = 289$ K and 0% RH) is about 237 W m^{-2}. A low cloud cover with substantial liquid water content and a small thermal inversion can easily push the value of the effective emissivity of the sky past unity, which pushes the longwave irradiation at the ground level to values near to, and sometimes above, 400 W m^{-2} for the same conditions. This difference in DLR is, of course, even larger at higher altitudes.

3.2. *Longwave irradiance ($\lambda > 4\mu m$) under cloudy-sky conditions*

To circumvent the vexing issue of having values of ε_{sky} larger than unity when thermal inversions are present, it is preferable to think of the cloudy atmosphere in terms of the effective optical depth of the entire atmosphere. The effective longwave transmissivity of the atmosphere brought to the reference of the ambient air temperature at the screening height T_e is simply $\tau_{\text{LW,sky}} = 1 - \varepsilon_{\text{LW,sky}}$, where the reasonable approximation of a nonreflective atmosphere to longwave radiation is assumed. The effective optical depth of the atmosphere for longwave radiation under clear skies is inversely calculated from

$$\tau_{\text{LW,sky}} = e^{-\mathcal{L}_{\text{LW,sky}}}, \quad (29)$$

and the daytime clear-sky optical depth at sea level $\mathcal{L}_{\text{LW,sky}}$ is now well approximated by the linear relationship on $p_w = P_w/P_o$ (Matsunobu and Coimbra, 2024),

$$\mathcal{L}_{\text{LW,clear day}} = 1.01 + 41.882\, p_w, \quad (30)$$

whereas the nighttime effective optical depth is well approximated as

$$\mathcal{L}_{\text{LW,clear night}} = 1.19 + 41.882\, p_w. \quad (31)$$

If we assume longwave cloud forcing to be additive to the clear-sky optical depth, which includes all main contributions to the greenhouse effect such as gases, aerosols and line overlaps (Li and Coimbra, 2019; Matsunobu and Coimbra, 2024), a clear scheme for classifying cloud forcing based on Eqs. (30) and (31) emerges as follows. At given conditions of screen temperature (T_e) and RH, clouds are classified within optical depth quartiles according to the complementary effective emissivity of the sky (1-$\varepsilon_{\text{LW,clear sky}}$), such that Q1 clouds are the least optically thick and Q4 are the most. Mathematically, this equates to defining a normalized effective optical depth for the cloudy sky as

$$r^*_{\text{LW,cloudy sky}} = \frac{\varepsilon_{\text{LW,cloudy sky}} - \varepsilon_{\text{LW,clear sky}}}{1 - \varepsilon_{\text{LW,clear sky}}}, \quad (32)$$

and since the effective total emissivity of the cloudy sky is

$$\begin{aligned} \varepsilon_{\text{LW,cloudy sky}} &= 1 - e^{-(\mathcal{L}_{\text{LW,clear sky}} + \mathcal{L}_{\text{LW,clouds}})} \\ &= (1 - \varepsilon_{\text{LW,clear sky}})\, r^*_{\text{LW,cloudy sky}} + \\ &\quad \varepsilon_{\text{LW,clear sky}}, \end{aligned} \quad (33)$$

the effective optical depth of the cloudy sky is recovered as

$$\begin{aligned}\mathcal{L}_{\mathrm{LW,cloudy\,sky}} &= \mathcal{L}_{\mathrm{LW,clear\,sky}} + \mathcal{L}_{\mathrm{LW,clouds}} \\ &= \mathcal{L}_{\mathrm{LW,clear\,sky}} - \ln(1 - r^{*}_{\mathrm{LW,cloudy\,sky}}) \,. \end{aligned} \quad (34)$$

Equation (33) assumes negligible longwave scattering by both clouds and aerosols, and thus the qualifier effective is applied. More detailed treatment of cloud and aerosol scattering effects can be found in Larson et al. (2020), Li et al. (2018) and Shakespeare and Roderick (2022).

The above classification scheme allows us to catalog cloud cover according to the effective longwave optical depth of the clouds in four quartiles (above the clear-sky optical depths) as follows:

$$\mathcal{L}_{\mathrm{LW,Q1}} = \text{from } \mathcal{L}_{\mathrm{LW,clear\,sky}} \text{ to } \mathcal{L}_{\mathrm{LW,clear\,sky}} + 0.288 \,, \quad (35)$$

$$\mathcal{L}_{\mathrm{LW,Q2}} = \text{from } \mathcal{L}_{\mathrm{LW,Q1}} \text{ to } \mathcal{L}_{\mathrm{LW,clear\,sky}} + 0.693 \,, \quad (36)$$

$$\mathcal{L}_{\mathrm{LW,Q3}} = \text{from } \mathcal{L}_{\mathrm{LW,Q2}} \text{ to } \mathcal{L}_{\mathrm{LW,clear\,sky}} + 1.386 \,, \quad (37)$$

$$\mathcal{L}_{\mathrm{LW,Q4}} = \text{from } \mathcal{L}_{\mathrm{LW,Q3}} \text{ to } +\infty \,, \quad (38)$$

where the Qi values correspond to different cloud or thermal inversion quartiles.

Note that the values above do not correspond exactly to emissivities in the quartiles 0.6–0.7, 0.7–0.8, and 0.8–0.9 for $p_w = 0$ (when $\varepsilon_{\mathrm{LW,clear\,sky}} \sim 0.6$) because the uncertainty in correlations (30) and (31) is higher for very low values of p_w, and therefore the quartiles are adjusted to fit the more likely (non-zero) values of relative water vapor partial pressure.

An example of the cloud classification scheme proposed here specifically for energy meteorology purposes is provided in Fig. (2). Given the typical value of about 10 W m^{-2} uncertainty of infrared pyrheliometer (PIR) measurements, the quartile classification proposed above should suffice for energy meteorology needs, including the determination of longwave fluxes from the panel to the ground, soil moisture evaporation rates, and other thermal and mass balances.

3.3. *Shortwave irradiance ($\lambda < 4\,\mu m$)*

Starting from the 1960s, decades of solar energy resourcing produced a number of empirical transposition models that allows us to estimate the shortwave irradiance striking on a sloped surface with an accuracy that is well matched to the uncertainties in both ground-based and remote sensing radiometry measurements. If beam irradiance G_b on a hori-

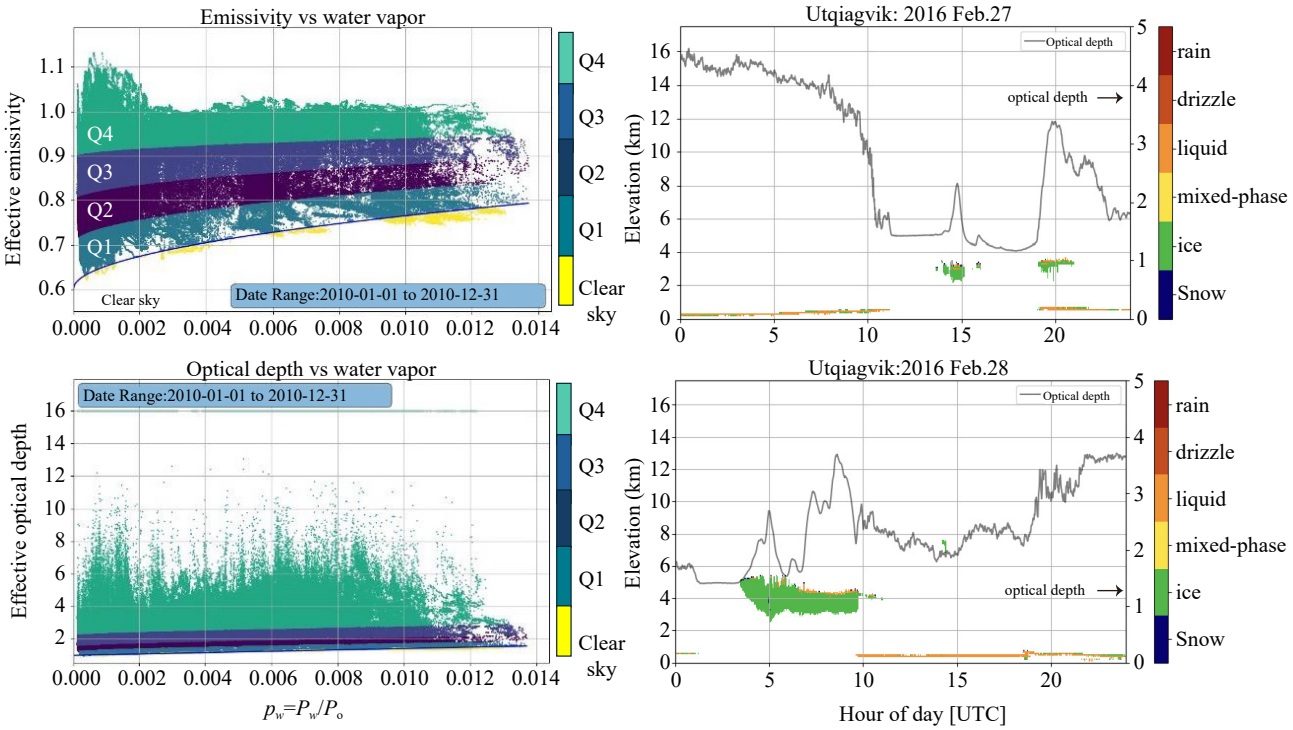

Fig. 2. Example of the classification scheme of effective emissivity and effective optical depth of the sky for energy meteorology applications. The top and bottom plates on the left side of the figure show effective emissivity and effective optical depth of the atmosphere for the entire year of 2010 collected for a site in Utqiagvik, Alaska (formerly known as Barrow, 71°17'N, 156°47'W). The colors on the left panels indicate clear sky (bottom) and the four quartiles of cloud cover and/or thermal inversions. Maximum optical depth values are capped at 16 instead of +∞. The two panels on the right correspond to two consecutive days in February 2016. Mixed-phase clouds are color-coded according to the classification scheme proposed by Shupe (2007) and Shupe (2011). The color code classification on the right panels does not correspond to the color code used on the left panels for each optically thick quartile. Note the strong influence of liquid water (orange) on the effective optical depth of the clouds on the right two panels.

zontal surface is measured, the direct irradiance on a sloped surface is just

$$G_{\mathrm{sw,direct}} = G_b \frac{\cos\theta}{\cos\theta_z}\,, \tag{39}$$

where the θ is the angle between the direct beam and the normal to the sloped surface, and θ_z is the solar zenith angle. Proper definition of these angles is necessary to represent the irradiation on sloped surfaces, and thus they are included here for completeness:

$$\begin{aligned}\cos\theta = &+\sin\delta\sin\phi\cos\beta - \sin\delta\cos\phi\sin\beta\cos\gamma + \\ &\cos\delta\cos\phi\cos\beta\cos\omega + \cos\delta\sin\phi\sin\beta\cos\gamma\cos\omega + \\ &\cos\delta\sin\beta\sin\gamma\sin\omega\,,\end{aligned} \tag{40}$$

and

$$\cos\theta_z = \cos\phi\cos\delta\cos\omega + \sin\phi\sin\delta\,. \tag{41}$$

The angle ϕ is the local latitude of the site, ω is the solar hour angle (angular apparent displacement of the Sun in the sky, morning negative, zero at solar noon, afternoon positive), and γ represents the surface azimuth angle (zero when pointing directly at the equator, growing positive to the east in the Northern Hemisphere). The angle δ is the Earth's axis declination, which for energy meteorology purposes can be calculated once a day. The cosine of the angle between the normal to the panel surface and the incident beam can also be conveniently expressed in terms of local angles, such as the solar azimuth γ_s, the panel azimuth angle γ, the solar azimuth θ_z, and the panel slope with the horizontal β angles (Duffie and Beckman, 2013):

$$\cos\theta = \cos\theta_z\cos\beta + \sin\theta_z\sin\beta\cos(\gamma_s - \gamma)\,. \tag{42}$$

In terms of the direct normal irradiance (DNI), which relates to the beam irradiation on a horizontal plane as $G_b = \mathrm{DNI}\cos\theta_z$, the direct irradiance on a sloped surface is simply $G_{\mathrm{sw,direct}} = \mathrm{DNI}\cos\theta$, so that the total shortwave irradiance on the top side of a sloped panel is given by

$$G_{\mathrm{sw,top}} = \mathrm{DNI}\cos\theta + \mathrm{GHI}\rho_{\mathrm{g}} F_{\mathrm{top-ground}} + \mathrm{DHI}\, R_{\mathrm{diff,top}}\,, \tag{43}$$

and on the bottom side as

$$\begin{aligned}G_{\mathrm{sw,bottom}} = &\,\mathrm{GHI}\,(\rho_{\mathrm{g}} F_{\mathrm{bottom-sunny}} + \rho_{\mathrm{s}} F_{\mathrm{bottom-shaded}}) + \\ &\mathrm{DHI}\, R_{\mathrm{diff,bottom}}\,,\end{aligned} \tag{44}$$

where the shortwave reflectivity (albedo) of the sunny and shaded portions of the ground surfaces are represented by ρ_g and ρ_s. The terms GHI and DHI refer to Global Horizontal Irradiance and Diffuse Horizontal Irradiance, respectively.

The diffusion transposition factor $R_{\mathrm{diff,side}}$ can be calculated using various transposition models (the specific value of $R_{\mathrm{diff,side}}$ for the two sides of the panel relies on adopting the correct view factor from the surface to the sky (see Appendix), as recently reviewed by Yang (2016). In his evaluation, Yang (2016) adapted an earlier version of the PEREZ transposition model for diffuse irradiation (Perez et al., 1987) and labeled it the PEREZ4 model. The PEREZ4 model was found to perform better than other empirical models by Yang (2016), and also performed well in comparison to Monte Carlo simulations by Li et al. (2020). A summarized formulation of the PEREZ4 model is reproduced in the Appendix. Cloud cover effects are either experimentally determined by measuring locally the different components of shortwave irradiation at the ground level (DNI, GHI and DHI), or estimated by resourcing data on cloudiness indices for both GHI and DNI [see, e.g., Duffie and Beckman (2013) and references within].

With $R_{\mathrm{diff,side}}$ values properly evaluated, the shortwave and the longwave irradiation fluxes are combined in each side of the panel so that

$$G_{\mathrm{top}} = G_{\mathrm{SW,top}} + G_{\mathrm{LW,top}}\,, \tag{45}$$

and

$$G_{\mathrm{bottom}} = G_{\mathrm{SW,bottom}} + G_{\mathrm{LW,bottom}}\,. \tag{46}$$

The value of the total irradiation fluxes above can be calculated by combining Eqs. (27) and (28) with Eqs. (43) and (44) for a gray panel. If the surfaces of the panel are further approximated as *selective*, i.e., with different gray properties in each part of the spectrum (shortwave and longwave), the SW and LW irradiation and radiosity fluxes are then modified by the respective SW and LW emissivities and used in Eq. (19) to recover the convective heat transfer coefficient for the panel. This can be done from modeling alone, or from a combination of POA irradiance and temperature measurements. Either way, the method allows us to evaluate the effective convective heat transfer coefficient for different panels in a large solar field.

The shortwave radiosity of a panel is only due to the effective shortwave reflectivity (albedo) of the panel since there is no measurable shortwave emission at operating temperatures. The thermal balance for the PV cell [Eq. (6)] can be adapted to compensate for the effective albedo by correcting the value of $(\tau\alpha)_{\mathrm{eff}}$. Equation (6) is first rewritten as

$$S - \eta_{\mathrm{PV}} G_{\mathrm{sw,top}} = U(T_{\mathrm{cell}} - T_e)\,, \tag{47}$$

where S is the shortwave irradiation absorbed by the PV cell through the cover system (encapsulation plus glass). The conversion efficiency η_{PV} is then *defined* as the ratio of electric power flux production in W m^{-2} to shortwave irradiation on the plane of the top cover (glass), also in W m^{-2}. There are two important corrections to be made to the value of $G_{\mathrm{SW,top}}$ in order to properly determine S. The first is an air-mass modifier factor M that accounts for the differentiated spectral absorption of different gases in the atmosphere at different slanted paths. This factor can be approximated for a variety of different cell and cover materials as a function of

the solar zenith angle (De Soto et al., 2006):

$$M(\theta_z) = 0.935823 + \frac{0.054289}{\cos\theta_z} - \frac{0.008677}{\cos\theta_z^2} + \frac{0.000527}{\cos\theta_z^3} - \frac{0.000011}{\cos\theta_z^4} . \quad (48)$$

The second correction refers to the angular dependence of the effective transmission-absorptance of the cover system on the incident radiation angle (Krauter and Hanitsch, 1996). This correction can be modeled by considering the optical properties of the semi-transparent cover and encapsulation plus the reflectivity of the PV cell, so that the absorbed shortwave irradiation is given by corrections to each mode of shortwave radiation (direct, ground reflected and diffuse):

$$S = M(\theta_z)(\tau\alpha)_n[\mathrm{DNI}\cos\theta\kappa_{\mathrm{DNI}}(\theta) + \mathrm{GHI}\rho_g F_{\mathrm{top-ground}}\kappa_{\mathrm{reflected}}(\theta) + \mathrm{DHI}R_{\mathrm{diff,top}}\kappa_{\mathrm{diffuse}}(\theta)] , \quad (49)$$

where $\kappa(\theta) \sim \kappa_{\mathrm{DNI}}(\theta) \sim \kappa_{\mathrm{reflected}}(\theta) \sim \kappa_{\mathrm{diffuse}}(\theta) \sim 1$ for $\theta < 50^o$. Note that $\kappa(\theta) \sim \kappa_{\mathrm{DNI}}(\theta) \sim \kappa_{\mathrm{reflected}}(\theta) \sim \kappa_{\mathrm{diffuse}}(\theta) < 1$ for $50^o < \theta < 75^o$. For even higher values of the incidence angle θ, the corrections proposed by King et al. (2004) should be used. A practical application of the corrections above under real outdoor conditions can be found in Gaglia et al. (2017).

If we assume that corrections for each component are near unity, Eq. (47) is further approximated as:

$$[M(\theta_z)(\tau\alpha)_{\mathrm{eff}} - \eta_{\mathrm{PV}}]G_{\mathrm{sw,top}} = U(T_{\mathrm{cell}} - T_e) , \quad (50)$$

which will be used in the next sections as a simplified model to calculate the global heat transfer coefficient U for the panel.

4. Determination of U for a PV panel

Proper determination of the global heat transfer coefficient U requires consideration of a thermal circuit such as the one depicted in Fig. 3. More elaborated versions of the thermal circuit (for example, with different values of T_e in each branch) may be required for certain applications. The equivalent conduction resistances R_{cond} are of the form δ/k, where δ is the thickness and k is the thermal conductivity of the material (both values for all materials involved are listed in Table 1).

In our simple model, the convective resistances $R_{\mathrm{conv,side}}$ are of the form $1/\bar{h}_{c,\mathrm{side}} = 1/\bar{h}_{c,\mathrm{panel}}$. The radiation resistances are also of the form $1/\bar{h}_{r,\mathrm{side}}$, but these require some additional thought because the irradiation is from sources at temperatures different than the air temperature T_e. The top radiation heat transfer coefficient equivalent is

$$\bar{h}_{r,\mathrm{top}} = \frac{\varepsilon_{\mathrm{LW,top}}(\sigma T_{\mathrm{top}}^4 - G_{\mathrm{LW,top}}) - \left([1 - \tau_{\mathrm{LW,top}}(\theta)]M(\theta_z) + 1\right)G_{\mathrm{SW,top}}}{T_{\mathrm{top}} - T_e} , \quad (51)$$

where $\varepsilon_{\mathrm{LW,top}}$ and $\tau_{\mathrm{LW,top}}$ are the longwave emissivity and transmissivity of the top (glass) cover. Note that the shortwave radiosity of the top surface is only due to reflection and is equal to the effective shortwave reflectivity times the shortwave irradiance. The effect of the shortwave radiosity for near-normal incidence ($\theta \sim 0$) is small and can be accounted for implicitly in the term $(\tau\alpha)_{\mathrm{eff}}$. For higher values of θ, the term multiplying $G_{\mathrm{SW,top}}$ must be examined and corrected accordingly, as indicated above. Similarly, the thermal resistance $R_{\mathrm{rad,cover}}$ can be neglected as the system absorption–transmission product includes the losses by thermal radiation through the glass, which are generally negligible in comparison to the conduction losses through the cover. The bottom radiation heat transfer coefficient is

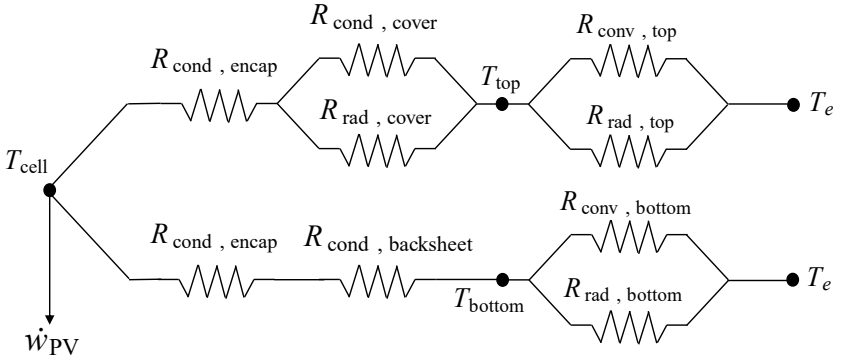

Fig. 3. Simple thermal resistance circuit for a PV panel including conduction, convection and radiation equivalent thermal resistances for both sides of the panel (top and bottom). The thermal circuit relates the average temperature of the PV cell (T_{cell}) to the temperature of the ambient air T_e. The radiation resistances are adjusted to T_e. Both branches are affected by T_{cell}, the photoelectric conversion flux $\dot{w}_{\mathrm{PV}}$, and the external heat fluxes.

$$\bar{h}_{r,\text{bottom}} = \frac{\varepsilon_{\text{bottom}}\sigma T_{\text{bottom}}^4 - G_{\text{bottom, absorbed}}}{T_{\text{bottom}} - T_e}\,, \qquad (52)$$

where again, $\varepsilon_{\text{bottom}}$ is the longwave emissivity of the backsheet material (say, ε_{PVF}), and $G_{\text{bottom,absorbed}}$ is the total (shortwave and longwave) absorbed irradiation by the bottom surface, $\varepsilon_{\text{SW,PVF}} G_{\text{SW,bottom}} + \varepsilon_{\text{LW,PVF}} G_{\text{LW,bottom}}$. The shortwave contributions may be entirely negligible depending on the optical properties of the backsheet material and time of the day.

5. Results and discussion

The above definitions combined with Eq. (50), plus the shortwave and longwave fluxes and the thermal circuit of Fig. 3 offer many potential pathways, both experimental and theoretical, for the determination of all thermal contributions to the fluxes to and from PV panels in large-scale solar farms. The thermal impact of large-scale power plants and the performance of the solar plants can thus be evaluated for different conditions. Take for example the (much simpler) empirical model developed at Sandia National Laboratories by King et al. (2004). In the Sandia model, which is often used in practice and is one of the models coded in to the U.S. Department of Energy's Solar Advisory Model (Gilman, 2015; King et al., 2004), the temperature difference between the PV cell and the backsheet is estimated as

$$T_{\text{cell}} - T_{\text{bottom}} = \frac{G_{\text{SW,top}}}{G_{\text{SW,ref}}}\Delta T\,, \qquad (53)$$

where $G_{\text{SW,ref}} = 1000$ W m^{-2} K, and ΔT is 3 K for the type of PV and mount described in Fig. 1. The same study found the difference between the backsheet temperature T_{bottom} and the ambient temperature T_e is approximated by

$$T_{\text{bottom}} - T_e = G_{\text{SW,top}}\, e^{a+bw_{10\text{m}}}\,, \qquad (54)$$

where $w_{10\,\text{m}}$ is the wind speed measured at 10 m height. Combining the empirically obtained relations given by Eqs. (53) and (54), with the model equation (50) provides an estimate for the global heat transfer coefficient U for different operating conditions as follows

$$U = \frac{[M(\theta_z)(\tau\alpha)_{\text{eff}} - \eta_{\text{PV}}]}{\frac{\Delta T}{G_{\text{SW,ref}}} + e^{a+bw_{10\,\text{m}}}}\,, \qquad (55)$$

where $\eta_{\text{PV}} = \dot{w}/G_{\text{SW,top}}$.

This relationship is of potential practical importance given that it estimates the global heat transfer coefficient U (which is less sensitive to fluctuating meteorological conditions than other quantities) to optical properties of the cover, the conversion efficiency of the module, and easily measured values of wind speed. The coefficients a and b are listed for different types of panels and mounts in King et al. (2004). For our case, $a = -3.56$, $b = -0.075$ s m^{-1}, and the global heat transfer coefficient is numerically expressed as

$$U = \frac{(M(\theta_z)(\tau\alpha)_{\text{eff}} - \eta_{\text{PV}})}{0.003 + e^{-3.56-0.075w_{10\,\text{m}}}}\,, \qquad (56)$$

which implies that, when the shortwave irradiation is near normal and the wind speed so high that convective losses are dominant, values of the order of $U \approx 100$ W m^{-2} K are reached (assume the numerator to be ~0.75 and the denominator to be ~0.0075 m^2 K^{-1} W^{-1} for maximum wind rating). This is a realistic value for highly convective environments when the efficiency of the PV cells is high under extreme wind load. On the other side of the range of possible wind speeds, the minimum value of U for natural convection losses only and near-normal irradiation is of the order $U \approx 24$ W m^{-2} K^{-1}, when the denominator in Eq. (56) approaches 0.0314 m^2 K^{-1} W^{-1}. While these two limiting values are realistic, the natural convection limit must be further scrutinized given the fact that natural convection flows do not conform to Newton's law of cooling in the sense that there is no invariant value of $\bar{h}_c$ for a given range of temperature differences (in other words, $\bar{h}_c$ is itself dependent on the temperature differences between the surface and the free-stream air). This simple hybrid model example highlights the use of empirical models and combining them with a detailed thermal balance model so that environmental impacts of solar farms can be studied in greater detail. Once the values of U and the temperatures in each side of the panels are estimated, the fluxes to and from the panels to the surrounding environment (ground and air) can be estimated under different environmental conditions through either modeling or experimentation, or a combination of both.

Finally, note that the model equations above are simplified to steady-state operation for simplicity of notation only. All heat fluxes can be measured or estimated as instantaneous rates and therefore transients can be easily accounted for in the formulation described in this work. A PV panel experiences rapid transients due to fluctuations in cloud cover and convective losses, but these transients can be easily incorporated in the model equations above by consideration of the appropriate thermal inertia (storage) properties (specific heat capacity, density and thermal conductivity) in Table 1. Lumped-capacity modeling is often assumed in such transient studies [see, e.g., Notton et al. (2005) and Jones and Underwood (2001)], but even the lumped capacity assumption, which is often valid, must be carefully considered as temperatures cannot always be considered uniform and steady along the surface or even across the thickness of the panels. For example, our simplified steady-state model, Eq. (50), can be modified for heat transfer imbalance between the two sides of the panel using a lumped-capacity heat balance, such as in Eq. (4), resulting in

$$\begin{aligned}&[M(\theta_z)(\tau\alpha)_{\text{eff}} - \eta_{\text{PV}}]\, G_{\text{sw,top}} - U(T_{\text{cell}} - T_e)\\ &= q_{\text{in}} - q_{\text{out}} - \dot{w}_{\text{PV}}\\ &= \rho_{\text{cell}}\, c_{\text{cell}}\, \delta_{\text{cell}} \frac{dT_{\text{cell}}}{dt}\,,\end{aligned} \qquad (57)$$

which can be used in conjunction with transient values of the radiative and convective fluxes and temperatures

described by the thermal circuit in Fig. 3 to calculate the time evolution of the the PV cell temperature according to fluctuations in the environmental conditions. The lumped-capacity assumption for the PV cell is justified since the effective Biôt number over the thickness of the cell is smaller than unity in situations of practical importance. This is not always the case for the entire PV panel, even across the thickness of the panel, much less through the entire surface. Note also that the PV conversion efficiency, η_{PV}, as well as key material properties, vary with temperature. Therefore, more elaborate nonlinear models can and should be used to evaluate the performance of solar panels and their impact on the surrounding environment.

6. Conclusions

This paper, which is somewhat comprehensive but not intended to be a complete review on the topic, provides a broad view of the type of modeling effort needed to properly account for the local heat balances to and from a solar farm. The emphasis is in the description of simple but effective models as opposed to providing definitive answers. A sample PV panel is used to illustrate the process of balancing convective and radiative (both shortwave and longwave) fluxes at the level of the PV panel, which is taken as the irreducible element of a solar farm. The methods discussed here are easily extended to heliostat fields.

Longwave radiation (both from and to the atmosphere and from and to the panel and ground) has received limited attention in previous studies, and therefore is treated in more detail here. A methodology to classify regional microclimates in terms of the effective optical depth of the cloudy atmosphere is proposed. The proposed classification of the cloud cover optical depth in 4 specific quartiles according to their impact on the DLR is appropriate given the approximations required by the heat transfer balances and the uncertainty in measuring DLR fluxes. There is an opportunity for energy meteorologists to map microclimates in terms of different quartiles for longwave optical depths of the sky. Such maps or tabled values can provide resourcing information complementary to the monthly, daily, or hourly averaged values of cloudiness or clearness indices for shortwave radiation used in the design, siting and management of solar power plants. References for progressive refinements of the detailed heat balances are provided. Once the global heat transfer coefficient is determined from a combination of modeling and field experimentation, the temperatures of the panel sides are determined for both daytime and nighttime, and their effect on soil humidity, local temperature and heat fluxes can be properly estimated for different operational and meteorological conditions.

This work is an attempt to motivate solar engineers and energy meteorologists to continue to study and reassess the environmental impact of large-scale solar farm deployment on sensitive desert habitats. It may very well be that the overall thermal impact of solar farms on these habitats is fairly low compared to other types of land use. However, it is the responsibility of the solar energy community to accurately model and report on those impacts, however small or large they might be. Clearly, much more research on this topic is needed. Our hope in writing this paper is that other researchers in the field will be motivated to develop progressively more sophisticated models that can be validated against field experiments in a variety of different microclimates.

Conflicts of interest. The author declares no conflicts of interest.

Data sharing policy The models and data that support the findings of this study are available from the corresponding author upon reasonable request.

Acknowledgements. The author is greatly indebted to Mr. Jason KNISS (U.S. Coast Guard) and Dr. Richard INMAN (UC San Diego) for processing the data and generating earlier versions of Fig. 2. Fruitful discussions with Prof. Lynn RUSSELL from the Scripps Institution of Oceanography at UC San Diego are also gratefully acknowledged. Prof. Dazhi YANG from the Harbin Institute of Technology asked me to look into the heat transfer impact of solar farms, and I am also indebted to him for the invitation to write this paper for AAS. Partial funding from the John Dove Isaacs Endowed Chair for Natural Philosophy in Engineering at UC San Diego is greatly appreciated.

APPENDIX: The PEREZ4 Transposition Model

The empirical transposition factor $R_{\text{diff,side}}$ in the PEREZ4 model is expressed as (Yang, 2016):

$$R_{\text{diff,side}} = (1-F_1)\,F_{\text{side-sky}} + F_1\frac{a'}{c'} + F_2\sin\beta\,, \tag{A1}$$

where $F_{\text{side-sky}}$ is equal to $F_{\text{top-sky}}$ for the top surface and equal to $F_{\text{bottom-sky}}$ for the bottom surface. The other coefficients are

$$\begin{aligned} a' &= 2(1-\cos\alpha_{\text{cs}})\chi_c\,; \\ c' &= 2(1-\cos\alpha_{\text{cs}})\chi_h\,; \end{aligned} \tag{A2}$$

$$\chi_c = \begin{cases} \psi_h\cos\theta, & \text{if } \theta < \pi/2-\alpha_{\text{cs}}\,, \\ \psi_h\psi_c\sin(\psi_c\alpha_{\text{cs}}), & \text{if } \theta_i \in [\pi/2\pm\alpha_{\text{cs}}]\,, \\ 0, & \text{otherwise}\,; \end{cases}$$

$$\chi_h = \begin{cases} \cos\theta_z, & \text{if } \theta_z < \pi/2-\alpha_{\text{cs}}\,, \\ \psi_h\sin(\psi_h\alpha_{\text{cs}}), & \text{otherwise}\,; \end{cases} \tag{A3}$$

$$\psi_c = \frac{\pi/2-\theta+\alpha_{\text{cs}}}{2\alpha_{\text{cs}}}\,;$$

$$\psi_h = \begin{cases} (\pi/2-\theta_z+\alpha)/2\alpha_{\text{cs}}, & \text{if } \theta_z > \pi/2-\alpha_{\text{cs}}\,, \\ 1, & \text{otherwise}\,; \end{cases} \tag{A4}$$

Table A1. Perez4 model coefficients for irradiance as functions of the sky clearness index (SCI).

SCI	F_{11}	F_{12}	F_{13}	F_{21}	F_{22}	F_{23}
[1,1.065)	−0.008	0.588	−0.062	−0.060	0.072	−0.022
[1.065,1.23)	0.130	0.683	−0.151	−0.019	0.066	−0.029
[1.23,1.5)	0.330	0.487	−0.221	0.055	−0.064	−0.026
[1.5,1.95)	0.568	0.187	−0.295	0.109	−0.152	−0.014
[1.95,2.8)	0.873	−0.392	−0.362	0.226	−0.462	0.001
[2.8,4.5)	1.133	−1.237	−0.412	0.288	−0.823	0.056
[4.5,6.2)	1.060	−1.600	−0.359	0.264	−1.127	0.131
[6.2, + ∞)	0.678	0.327	0.250	0.156	1.377	0.251

the brightness coefficients for the circumsolar (cs) radiation (F_1) and for the horizon (F_2) are found for specific ranges of values of the sky clearness index SCI in Table A1:

$$\begin{aligned} F_1 &= \max[0, F_{11}(\mathrm{SCI}) + F_{12}(\mathrm{SCI})\,\Delta + \theta_z F_{13}(\mathrm{SCI})], \\ F_2 &= F_{21}(\mathrm{SCI}) + F_{22}(\mathrm{SCI})\Delta + F_{23}(\mathrm{SCI})\theta_z, \\ \mathrm{SCI} &= (\mathrm{DHI} + \mathrm{DNI})/\mathrm{DHI}, \text{ and} \\ \Delta &= \mathrm{DHI}/(G_o \cos\theta_z), \end{aligned} \tag{A5}$$

where α_{cs} is the circumsolar half angle [normally assumed to be 25°; see Perez et al. (1987)], and G_{on} is the extraterrestrial irradiance on a normal plane to the beam, $G_{on} \sim 1{,}361(1 + 2e_E \cos(360n/365)$, where n is the nth day of the year and e_E is the eccentricity of the Earth's orbit (~0.017). The values of the sub-coefficients F_{ij} are also given in Table A1. Note that the circumsolar coefficient F_1 can usually be considered null for the bottom side of the panel. The values of θ_z in the expressions for F_1 and F_2 are expressed in radians.

REFERENCES

Barron-Gafford, G. A., R. L. Minor, N. A. Allen, A. D. Cronin, A. E. Brooks, and M. A. Pavao-Zuckerman, 2016: The photovoltaic heat island effect: Larger solar power plants increase local temperatures. *Scientific Reports*, **6**, 35070, https://doi.org/10.1038/srep35070.

Berdahl, P., 2021: Retrospective on the resource for radiative cooling. *Journal of Photonics for Energy*, **11**, 042106, https://doi.org/10.1117/1.jpe.11.042106.

De Soto, W., S. A. Klein, and W. A. Beckman, 2006: Improvement and validation of a model for photovoltaic array performance. *Solar Energy*, **80**, 78–88, https://doi.org/10.1016/j.solener.2005.06.010.

Duffie, J. A., and W. A. Beckman, 2013: *Solar Engineering of Thermal Processes*. 4th ed. John Wiley & Sons.

Fan, C. X., and X. L. Huang, 2021: Direct impact of solar farm deployment on surface longwave radiation. *Environmental Research Communications*, **3**, 125006, https://doi.org/10.1088/2515-7620/ac40f1.

Fathi, N. Y., and A. Samer, 2016: View factors of flat solar collectors array in flat, inclined, and step-like solar fields. *Journal of Solar Energy Engineering*, **138**, 061005, https://doi.org/10.1115/1.4034549.

Gaglia, A. G., S. Lykoudis, A. A. Argiriou, C. A. Balaras, and E. Dialynas, 2017: Energy efficiency of PV panels under real outdoor conditionse-An experimental assessment in Athens, Greece. *Renewable Energy*, **101**, 236–243, https://doi.org/10.1016/j.renene.2016.08.051.

Gilman, P., 2015: SAM photovoltaic model technical reference. Techn. Rep. DE-AC36-08GO28308.

Hernandez, R. R., and Coauthors, 2014: Environmental impacts of utility-scale solar energy. *Renewable and Sustainable Energy Reviews*, **29**, 766–779, https://doi.org/10.1016/j.rser.2013.08.041.

Hu, A. X., and Coauthors, 2016: Impact of solar panels on global climate. *Nature Climate Change*, **6**, 290–294, https://doi.org/10.1038/nclimate2843.

Jones, A. D., and C. P. Underwood, 2001: A thermal model for photovoltaic systems. *Solar Energy*, **70**, 349–359, https://doi.org/10.1016/S0038-092X(00)00149-3.

King, D. L., W. E. Boyson, and J. A. Kratochvil, 2004. Photovoltaic array performance model. Techn. Rep. SAND 2004-3535.

Krauter, S., and R. Hanitsch, 1996: Actual optical and thermal performance of PV-modules. *Solar Energy Materials and Solar Cells*, **41–42**, 557–574, https://doi.org/10.1016/0927-0248(95)00143-3.

Larson, D. P., M. Y. Li, and C. F. M. Coimbra, 2020: SCOPE: Spectral cloud optical property estimation using real-time GOES-R longwave imagery. *Journal of Renewable and Sustainable Energy*, **12**, 026501, https://doi.org/10.1063/1.5144350.

Li, M. Y., and C. F. M. Coimbra, 2019: On the effective spectral emissivity of clear skies and the radiative cooling potential of selectively designed materials. *International Journal of Heat and Mass Transfer*, **135**, 1053–1062, https://doi.org/10.1016/j.ijheatmasstransfer.2019.02.040.

Li, M. Y., Y. J. Jiang, and C. F. M. Coimbra, 2017: On the determination of atmospheric longwave irradiance under all-sky conditions. *Solar Energy*, **144**, 40–48, https://doi.org/10.1016/j.solener.2017.01.006.

Li, M. Y., Z. Y. Liao, and C. F. M. Coimbra, 2018: Spectral model for clear sky atmospheric longwave radiation. *Journal of Quantitative Spectroscopy and Radiative Transfer*, **209**, 196–211, https://doi.org/10.1016/j.jqsrt.2018.01.029.

Li, M. Y., Z. Y. Liao, and C. F. M. Coimbra, 2020: Spectral solar irradiance on inclined surfaces: A fast Monte Carlo approach. *Journal of Renewable and Sustainable Energy*, **12**, 053705, https://doi.org/10.1063/5.0011635.

Martin, M., and P. Berdahl, 1984: Summary of results from the spectral and angular sky radiation measurement program. *Solar Energy*, **33**, 241–252, https://doi.org/10.1016/0038-092X(84)90155-5.

Masson, V., M. Bonhomme, J. L. Salagnac, X. Briottet, and A.

Lemonsu, 2014: Solar panels reduce both global warming and urban heat island. *Frontiers in Environmental Science*, **2**, 14, https://doi.org/10.3389/fenvs.2014.00014.

Matsunobu, L. M., and C. F. M. Coimbra, 2024: On effective spectral wideband models for clear sky atmospheric emissivity and transmissivity. *J. Geophys. Res.*, **129**, e2023JD039798, https://doi.org/10.1029/2023JD039798.

Mills, A. F., and C. F. M. Coimbra, 2015: *Basic Heat and Mass Transfer*. 3rd ed. Temporal Publishing.

Millstein, D., and S. Menon, 2011: Regional climate consequences of large-scale cool roof and photovoltaic array deployment. *Environmental Research Letters*, **6**, 034001, https://doi.org/10.1088/1748-9326/6/3/034001.

Nassar, Y. F., H. J. El-Khozondar, S. O. Belhaj, S. Y. Alsadi, and N. M. Abuhamoud, 2022: View factors in horizontal plane fixed-mode solar PV fields. *Frontiers in Energy Research*, **10**, 859075, https://doi.org/10.3389/fenrg.2022.859075.

Nemet, G. F., 2009: Net radiative forcing from widespread deployment of photovoltaics. *Environmental Science & Technology*, **43**, 2173–2178, https://doi.org/10.1021/es801747c.

Notton, G., C. Cristofari, N. Mattei, and P. Poggi, 2005: Modelling of a double-glass photovoltaic module using finite differences. *Applied Thermal Engineering*, **25**, 2854–2877, https://doi.org/10.1016/j.applthermaleng.2005.02.008.

Perez, R., R. Seals, P. Ineichen, R. Stewart, and D. Menicucci, 1987: A new simplified version of the Perez diffuse irradiance model for tilted surfaces. *Solar Energy*, **39**, 221–231, https://doi.org/10.1016/S0038-092X(87)80031-2.

Shakespeare, C. J., and M. L. Roderick, 2021: The clear-sky downwelling long-wave radiation at the surface in current and future climates. *Quart. J. Roy. Meteor. Soc.*, **147**, 4251–4268, https://doi.org/10.1002/qj.4176.

Shakespeare, C. J., and M. L. Roderick, 2022: Diagnosing instantaneous forcing and feedbacks of downwelling longwave radiation at the surface: A simple methodology and its application to CMIP5 models. *J. Climate*, **35**, 3785–3801, https://doi.org/10.1175/JCLI-D-21-0865.1.

Shupe, M. D., 2007: A ground-based multisensor cloud phase classifier. *Geophys. Res. Lett.*, **34**, L22809, https://doi.org/10.1029/2007GL031008.

Shupe, M. D., 2011: Clouds at arctic atmospheric observatories. Part Ⅱ: Thermodynamic phase characteristics. *J. Appl. Meteorol. Climatol.*, **50**, 645–661, https://doi.org/10.1175/2010JAMC2468.1.

Smith, S. E., B. J. Stanislawski, B. K. Eng, N. Ali, T. J. Silverman, M. Calaf, and R. B. Cal, 2022a: Viewing convection as a solar farm phenomenon broadens modern power predictions for solar photovoltaics. *Journal of Renewable and Sustainable Energy*, **14**, 063502, https://doi.org/10.1063/5.0105649.

Smith, S. E., B. Viggiano, N. Ali, T. J. Silverman, M. Obligado, M. Calaf, and R. B. Cal, 2022b: Increased panel height enhances cooling for photovoltaic solar farms. *Applied Energy*, **325**, 119819, https://doi.org/10.1016/j.apenergy.2022.119819.

Wang, F., and Coauthors, 2023: Heat-dissipation performance of photovoltaic panels with a phase-change-material fin structure. *Journal of Cleaner Production*, **423**, 138756, https://doi.org/10.1016/j.jclepro.2023.138756.

Yang, D. Z., 2016: Solar radiation on inclined surfaces: Corrections and benchmarks. *Solar Energy*, **136**, 288–302, https://doi.org/10.1016/j.solener.2016.06.062.